NeuroImage 201 (2019) 116008

Contents lists available at ScienceDirect

NeuroImage

journal homepage: www.elsevier.com/locate/neuroimage

Dynamic causal modeling for calcium imaging: Exploration of differential effective connectivity for sensory processing in a barrel cortical column

Kyesam Jung [a,b,1], Jiyoung Kang [a,b,1], Seungsoo Chung [c,d], Hae-Jeong Park [a,b,d,e,*]

[a] Center for Systems and Translational Brain Sciences, Institute of Human Complexity and Systems Science, Yonsei University, Seoul, Republic of Korea
[b] Department of Nuclear Medicine, Yonsei University College of Medicine, Seoul, Republic of Korea
[c] Department of Physiology, Yonsei University College of Medicine, Seoul, Republic of Korea
[d] BK21 PLUS Project for Medical Science, Yonsei University College of Medicine, Seoul, Republic of Korea
[e] Department of Cognitive Science, Yonsei University, Seoul, Republic of Korea

ARTICLE INFO

Keywords:
Dynamic causal modeling
Calcium imaging
Barrel cortex
Effective connectivity
Sensory processing
Top-down modulation

ABSTRACT

Multi-photon calcium imaging (CaI) is an important tool to assess activities of neural populations within a column in the sensory cortex. However, the complex asymmetrical interactions among neural populations, termed effective connectivity, cannot be directly assessed by measuring the activity of each neuron or neural population using CaI but calls for computational modeling. To estimate effective connectivity among neural populations, we proposed a dynamic causal model (DCM) for CaI by combining a convolution-based dynamic neural state model and a dynamic calcium ion concentration model for CaI signals. After conducting a simulation study to evaluate DCM for CaI, we applied it to an experimental CaI signals measured at the layer 2/3 of a barrel cortical column that differentially responds to hit and error whisking trials in mice. We first identified neural populations and constructed computational models with intrinsic connectivity of neural populations within the layer 2/3 of the barrel cortex and extrinsic connectivity with latent external modes. Bayesian model inversion and comparison shows that interactions with latent inhibitory and excitatory external modes explain the observed CaI signals within the barrel cortical column better than any other tested models, with a single external mode or without any latent modes. The best model also showed differential intrinsic and extrinsic effective connectivity between hit and error trials in the functional hierarchy. Both simulation and experimental results suggest the usefulness of DCM for CaI in terms of exploration of hierarchical interactions among neural populations observed in CaI.

1. Introduction

In the exploration of the neural interactions within a cortical column, multi-photon calcium imaging (CaI) is an important tool to obtain information regarding distributions of neurons (in superficial layers) and to assess activities of neural populations. CaI allows exploration of the functional tuning of each neuron while perceiving a stimulus (Ohki et al., 2005) or conducting a task (Guo et al., 2014; Peron et al., 2015), using relatively high speed imaging techniques (Grewe et al., 2010; Helassa et al., 2016). Using CaI, it is also possible to investigate complex interactions among multitudes of neurons within a cortical column in detail, which otherwise is not generally possible.

A cortical column, as a functional unit of sensory perception, is understood to process bottom-up signals by integrating them with top-down information via the populations of excitatory neurons and inhibitory interneurons distributed across layers of the cortical column. The functional architecture of these processes is reflected in recent canonical micro-circuitry models that include interactions within three or four neural subpopulations in the cortical column, in association with externals (Bastos et al., 2012; Douglas and Martin, 1991; Haeusler and Maass, 2006). These populations are considered to interact with others asymmetrically through feed-forward and feed-backward connections (Chaudhuri et al., 2015; Friston, 2018; Mesulam, 1998; Park and Friston, 2013), which is supported by neuroanatomical studies (Markov et al., 2014). Since the interactions among neural populations within a neural column (i.e., intrinsic connectivity) and those with neural populations

* Corresponding author. Department of Nuclear Medicine, Department of Psychiatry, Yonsei University College of Medicine, Department of Cognitive Science, Yonsei University, Center for Systems and Translational Brain Sciences, Institute of Human Complexity and Systems Science, Yonsei University 50-1, Yonsei-ro, Sinchon-dong, Seodaemun-gu, Seoul, 03722, Republic of Korea.
E-mail address: parkhj@yonsei.ac.kr (H.-J. Park).
[1] equally contributed authors.

https://doi.org/10.1016/j.neuroimage.2019.116008
Received 24 December 2018; Received in revised form 24 June 2019; Accepted 9 July 2019
Available online 10 July 2019

outside the column (extrinsic) are generally reciprocal and asymmetrical, they can be better described by effective connectivity than by functional synchrony (Friston, 1994). However, the effective connectivity among neural populations, occurring at the cortical column in the sensory cortex, cannot be directly assessed by measuring the activity of each neuron using CaI but calls for computational modeling.

In the investigation of the neural interactions using computational modeling, CaI has innate limitations due to the transmission limit of light and the limitation in the spatial coverage for a given spatial resolution; CaI can primarily measure neural activity in the superficial layers but not in the deep layers in vivo. Furthermore, CaI cannot measure activity across multiple columns at a single-neuron level (i.e., trade-off between coverage and spatial resolution). Since the cortical column itself does not act alone but integrates signals received from outside the column, we cannot fully understand the activity and interactions among neurons within the column through CaI measurements at a shallow portion (usually the layer 2/3) of a single column. The lack of measurements at the deeper layers and at regions outside the column demands estimation of hitherto unobserved data (such as hidden states or latent variables) under constraints of coevolving hidden-state, and connectivity estimation through observed data.

The purpose of the current study is to propose a method to explore effective connectivity among neural populations within a barrel cortical column using CaI, and to test the need for external modulation in a column of the barrel cortex during a task. For modeling columnar connectivity using CaI, we modeled the neural encoding at the mesoscopic level by clustering neurons into several groups according to the waveforms of their CaI signals. This approach is based on the *population coding* hypothesis, which states that the brain encodes sensory information in the neural population (Pasupathy and Connor, 2002; Pouget et al., 2000). It begins with estimation of the number of neural populations from a multitude of neurons. To estimate effective connectivity among neural populations, we propose a type of dynamic causal model (DCM) (Friston et al., 2003, 2007) for CaI by combining a convolution-based neural state model modified from Moran et al. (2013) and a realistic CaI observation model (Rahmati et al., 2016). The proposed approach differs from the model of Rosch et al. (2018), where a fixed kernel function is used for CaI observation.

We applied the proposed modeling scheme in the exploration of integrative processing within a column in the barrel cortex using a public dataset (https://crcns.org/data-sets/ssc/ssc-2/about-ssc-2). The dataset contains CaI data of a column of the mouse barrel cortex during a pole localization task, responding to changes in the curvature and angle of a whisker in the localization step, which involved licking a reward port to receive water drops (Peron et al., 2015). In the original paper, Peron et al. (2015) reported that the proportions of representative neurons for touch and whisking, and their characters are stable during learning. Moreover, the touch and whisking behaviors showed different neural activity maps in a barrel cortical column. The authors concluded that the neurons in the layer 2/3 of the barrel cortex are organized to encode sensory inputs from whiskers. However, they did not fully explore how neural populations in the layer 2/3 of the barrel cortex respond differently to two different types of behaviors, i.e., those during hit and error trials. Thirsty mice successfully lick a reward port to receive water drops in the hit trials but failed to lick a correct port even though they touched the target pole in the error trials. In the error trials, information processing of the sensory input did not lead to rewards. The contrast between hit and error trials for the same sensory input might be caused from differential sensory processing in the effective connectivity of the barrel cortical column.

What is the difference in the effective connectivity among neural populations when the sensory cortex processes perception to successfully receive rewards or fail? The answer to this question may lie in the top-down and bottom-up interactions among neural populations in a cortical column. Specifically, the difference in success or failure would be reflected in the intrinsic effective connectivity among neural components in a column with differential extrinsic connectivity with externals. To test this hypothesis, we constructed and evaluated computational models with intrinsic connectivity of neural populations within the layer 2/3 of the barrel cortex and extrinsic connectivity with latent external modes (corresponding to the bottom-up and top-down processes).

The current paper is composed of four parts: 1) processing of CaI signals and extraction of neural populations; 2) introduction of DCM for CaI and explaining DCM models of neural populations for hit and error trials; 3) simulation and validation of DCM for CaI; and 4) evaluation of models, followed by the discussion on the use of computational models for explaining hits and errors in the perspective of extrinsic signaling within the layer 2/3 of a barrel cortical column.

2. Methods

2.1. Experimental data

We analyzed functional CaI data of neuronal responses in the barrel cortex evoked by a single whisking cycle (Guo et al., 2014; Peron et al., 2015), which is available from a public database (https://crcns.org/data-sets/ssc/ssc-2). Briefly explaining the data, six 6–8-week old emx1-Cre X LSL-H2B-mCherry mice, which had red nuclei in excitatory neurons and glial cells (Gorski et al., 2002), were used. They were infected with AAV2/1 syn-GCaMP6s (Chen et al., 2013) to indicate the concentration of cytosolic calcium ions in neurons; CaI data from $600 \times 600\ \mu m^2$ (512×512 pixels) imaging planes, separated by 15 μm in depth, were acquired at 7 Hz while each pre-trained mouse performed a task. In the task, a target pole appears within the ambit of whisking of a single whisker. The angle and the curvature of a whisker and the onset times of protracting and retracting touches were acquired at 500 Hz. Posterior and anterior locations of the target pole indicate the right and left lick-ports which supply water drops as rewards. The task was to select a lick-port that will supply water drops in a given trial. The hit trial indicates that the thirsty mice successfully chose a lick-port which supplies water drops. During the error trials, the mice failed to choose the correct lick-port. The total numbers of hit-right and error-right trials conducted by all the five mice were 8908 and 5002, respectively. The task and data have been described in detail by Guo et al. (2014) and Peron et al. (2015), and preprocessing of CaI signals has been described by Huber et al. (2012). The preprocessing steps described in Huber et al. (2012) include motion correction, segmentation of neurons, fluorescence signal extraction at each neuron and estimation of baseline and signal changes. The fluorescence signal change $(F - F_0)/F_0$ was computed using the estimated baseline F_0.

To examine trial type-dependent effective connectivity among the neural populations in a barrel column, we divided the trials into hit and error types and conducted computational modeling for these two performances. The procedure for signal processing for computational modeling is presented in Fig. 1 and is explained in the following sections.

2.2. Classification of inhibitory and excitatory cells

We selected responsive neurons based on the empirical criterion that the duration of high-signal changes ($\Delta F/F$) (higher than 1) should exceed at least 5% of the total data points (see Fig. 2a). We then classified inhibitory and excitatory neurons based on red fluorescence channel images (mCherry; 675/70 emission filter, Chroma). A cell segment (provided in the dataset) was identified as excitatory if the intensity of pixels inside the target cell segment (H2B-mCherry) was brighter than its surroundings (neuropil), and was otherwise considered inhibitory (Gorski et al., 2002). The syn-GCaMP6s positive indicates that the cell is a neuron (Chen et al., 2013). H2B-mCherry positive (brighter inside of a cell than the surrounding) indicates that the cell is an excitatory neuron or a glial cell (Gorski et al., 2002). Therefore, cells with H2B-mCherry positive and syn-GCaMP6s positive were regarded as excitatory neurons while cells with H2B-mCherry negative and syn-GCaMP6s positive were assigned as inhibitory neurons. Using this criterion, 595 excitatory

neurons and 151 inhibitory neurons were manually identified from all the five mice.

2.3. Identification of neural populations

We analyzed hit- and error-trials in the right-target pole condition because the mice were trained to employ a whisking strategy that maximizes the number of touches for the "right-target" condition (hit the pole while whisking toward the right) and minimizes the number of touches for the "left-target" condition (Guo et al., 2014). We first divided all trials into hit- and error-performing trials in the right-target condition. We then extracted evoked calcium signals by averaging the traces of calcium signals for the hit trials and error trials separately at each neuron using the following steps. To derive an evoked calcium signal in reference to the onset time of the first touch (defined in the behavioral data), we aligned calcium signals of all trials with respect to their acquisition times on the axis with a temporal bin of 2 m s (500 Hz) from the onset time at each neuron. We then averaged the temporally aligned samples of all trials for each performance type (hit or error), over sliding windows with a window size of 6/14 s at a temporal step of 71.4 ms (14 Hz), to estimate an evoked calcium signal (Fig. 2b).

To identify neural populations responding synchronously (often termed modes), we concatenated evoked calcium signals for hit and error trials at each neuron. We then applied Principal component analysis (PCA) to the concatenated evoked calcium signals of all the excitatory neurons (dimension: N_e neurons $\times$ [T_{hit} + T_{error}] total number of time series) to reduce temporal dimensions. PCA was again applied to the concatenated evoked calcium signals of all the inhibitory neurons ($N_i \times$ [T_{hit} + T_{error}]). The numbers of excitatory and inhibitory neural populations were determined using the following approach. First, 95% explainable principal component (PC) weights (for concatenated hit and error trials, dimension: $P_{e/i}$) for $N_{e/i}$ neurons were used as feature vectors for *k-means* clustering of all neurons in each excitatory or inhibitory group.

To find a reliable set of neural populations, we repeated k-means clustering 10,000 times for PC weights of neurons [$N_{e/i}$ x $P_{e/i}$] with an empirical K = 8 as an initial number of clusters for each neuron type (excitatory/inhibitory). Since every executions of k-means clustering show variations in the clustering result, we evaluated the frequency for each pair of neurons being a same cluster among 10,000 k-means clustering executions. This composed a frequency adjacency matrix for all pairs of excitatory (or inhibitory) neurons. The element (edge) of the frequency adjacency matrix indicates how robustly two nodes (neurons) are clustered as a same cluster. From the frequency adjacency matrix, the *modularity optimization* algorithm (Newman and Girvan, 2004) in the Brain Connectivity Toolbox (Rubinov and Sporns, 2010) (Fig. 3a and b) identified 5 and 4 modes for excitatory and inhibitory neurons while maximizing the modularity index (Q).

2.4. Dynamic causal modeling: neural state model

In order to construct computational models of interactions among the neural populations observed in CaI, we followed a DCM framework (Friston et al., 2007) implemented in SPM12 toolbox (https://www.fil.ion.ucl.ac.uk/spm/). We extended a convolution-based model (Jansen and Rit, 1995; Moran et al., 2013) to describe the state dynamics of each neural population. In the modeling, activity of a neural population (i.e., mode) was considered as that of an equivalent neuron for the population.

In the convolution-based model for the neural state, a sigmoid function $\sigma(v)$ is used as a firing-rate transfer function that converts a mean membrane potential of neurons in a population (mode) to a firing rate in the neural population. Then, the firing rate influences a post-synaptic potential through a synaptic kernel. Fig. 4 illustrates the dynamics of the states of three neural populations (or modes) throughout a convolution-based model. The convolution-based model can be expressed as an ordinary differential equation of cross-membrane current at a neural population:

$$i_n^{\cdot} = \frac{di_n}{dt} = \kappa_n H_n \left(\sum_{m \in M_n} \gamma_{nm} \sigma_m(v_m) + I_n \right) - 2\kappa_n i_n - \kappa_n^2 v_n \quad [1]$$

$$\sigma(v) = \frac{f_{max}}{1 - e^{-R(v - v_0)}}$$

Here, i_n is the cross-membrane current of a post-synaptic neural population n; v_m and v_n are the cross-membrane potentials of neural populations m and n. M_n indicates all neural populations that have connections to a neural population n. γ_{nm} is the effective connectivity from a neural population m to the neural population n. I_n is an external input on the post-synaptic neural population n. V_0 is the post-synaptic potential that achieves a 50% firing rate of a neural population (Jansen and Rit, 1995). κ represents the inversion of the time constant of the synaptic kernel, and H is the maximal post-synaptic potential. The cross-membrane potential for each neural population is updated by the following equation:

$$v_n = \frac{dv_n}{dt} = i_n \quad [2]$$

The assumption in Eq. (2) is that the cross-membrane current equals the change in the cross-membrane potential if we consider the membrane capacitance to be a constant value (Hodgkin and Huxley, 1952). In contrast to a conductance model for a single neuron (Hodgkin and Huxley, 1952), which contains intrinsic parameters for cross-membrane sodium and potassium ion currents to generate action potential, the v in Eqs. (1) and (2) describes a mean cross-membrane potential of a populaton. Following the previous works (Jansen and Rit, 1995; Moran et al., 2013), we differentiated excitatory and inhibitory neural populations in the computational model, which induce depolarization and hyperpolarization of membrane potentials of the target neural populations.

For the driving input, we referred to an average touch fraction curve during the sample period (Guo et al., 2014; Peron et al., 2015). After the first touch, a burst of touches was observed until the target pole disappeared (1 s). Thus, we applied a boxcar function of 1-s duration as a driving input for the subsequent neural populations. The weighted assignment of the external input to each node was specified in the parameter vector C (Fig. 4).

2.5. Dynamic causal modeling: CaI observation model

The observation model for CaI was composed of a differential equation regarding the concentration of calcium ions ([Ca^{2+}]) and a transformation from the calcium ion concentration to the calcium signal (Rahmati et al., 2016). The calcium dynamics (see Fig. 5) can be described by the following equation:

$$\frac{d}{dt}\left[Ca^{2+}\right] = -\kappa_{Ca} g_{Ca} \cdot (v - E_{Ca}) \cdot \sigma(v - V_{HVA}) - \frac{[Ca^{2+}] - [Ca^{2+}]_{base}}{\tau_{Ca}} \quad [3]$$

Here, the parameter κ_{Ca} is the conversion ratio from a calcium ion current to its concentration per time unit; g_{Ca} represents the maximal conductance of calcium ions, E_{Ca} is the reversal potential of calcium ion, the membrane potential v in Eq. (2) and Fig. 4 is an input to the calcium ion concentration dynamics, and τ_{Ca} is a time constant. Following Rahmati et al. (2016), we employed a high-voltage-activated calcium channel (HVA), having a half-activation voltage (V_{HVA}) for a sigmoidal function, $\sigma(v - V_{HVA})$ (Table 1). The transformation from a calcium ion concentration to a calcium signal is described by the following equation:

$$g\left(\left[Ca^{2+}\right]\right) = \kappa_F \frac{[Ca^{2+}]}{[Ca^{2+}] + K_d} + d_F \quad [4]$$

where κ_F, K_d, and d_F are scale, dissociation, and offset parameters. The parameters in Eq. (3) and Eq. (4) that describe calcium dynamics were

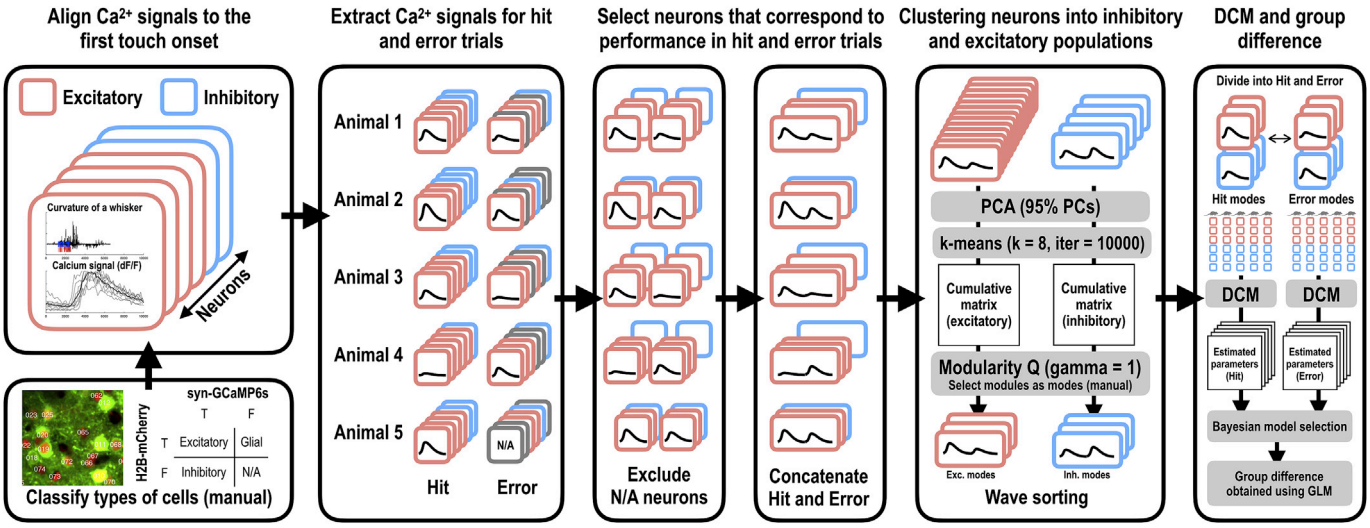

Fig. 1. Procedure for signal processing and dynamic causal modeling for calcium imaging. It consists of waveform sorting, clustering signals according to hit and error trials and according to inhibitory and excitatory neural populations, and dynamic causal modeling to estimate the difference in effective connectivity for hit and error trials at the group level. N/A: not available, PCA: principal component analysis, Exc.: excitatory, Inh.: inhibitory, DCM: dynamic causal modeling, and GLM: general linear model.

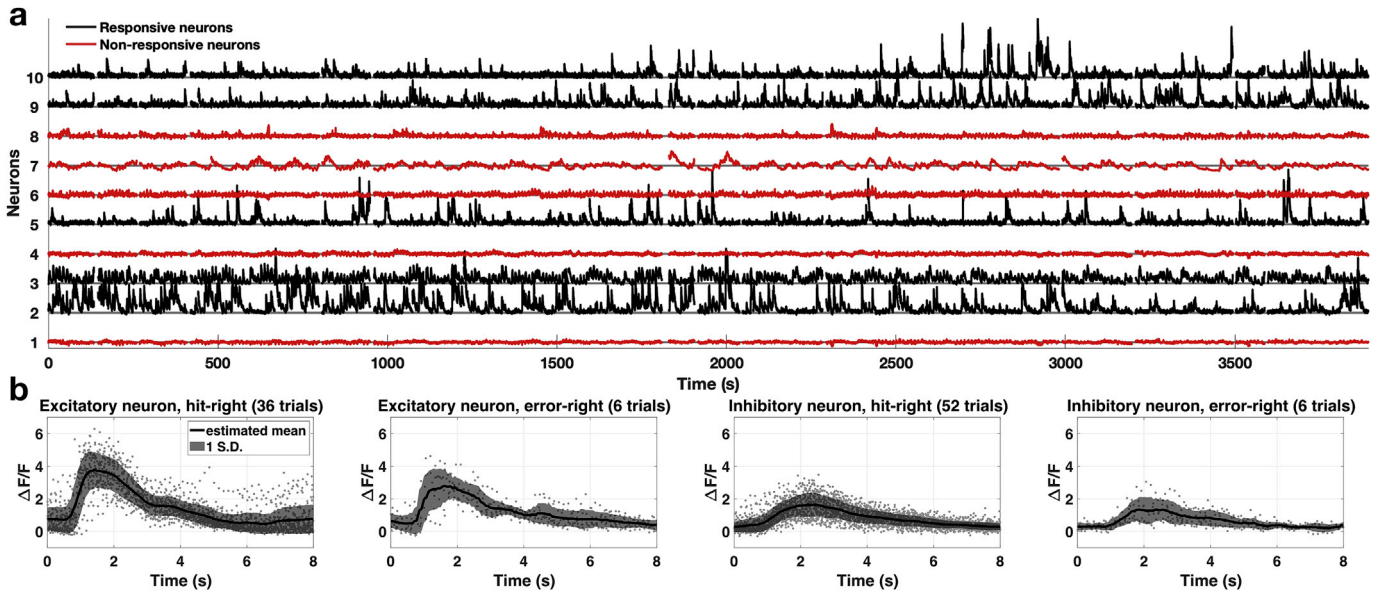

Fig. 2. Identification of responsive neurons and extraction of evoked calcium signals. (a) displays calcium signals ($\Delta F/F$) across a whole session. Black lines represent signals from responsive neurons that show responses during whole trials. Red lines represent signals from neurons that are not active for the task. (b) shows examples of evoked calcium signals from responsive excitatory and inhibitory neurons during hit and error trials, aligned to the onset time of the first touch.

obtained from previous studies (Rahmati et al., 2016; Yaksi and Friedrich, 2006). Fig. 5 presents simulation results for calcium ion concentrations and CaI signals generated using the observation model with different inputs (membrane potentials having different amplitudes and shapes).

2.6. Computational models for a barrel column

The sensory processing in the layer 2/3 is known to integrate bottom-up afferent inputs from the layer 4 (L4, excitable mode), which is evoked mainly by thalamocortical signals (Petersen and Sakmann, 2001), and the top-down inputs (excitable and inhibitable) from cortical regions outside the cortical column. We hypothesized that the difference in the hit and error trials is associated with differential processing of intrinsic and extrinsic effective connectivity within the barrel cortical column.

To explain the mechanism of hit and error trials with respect to effective connectivity for top-down and bottom-up processing (Bastos et al., 2012; Douglas and Martin, 2004; Zagha et al., 2016), we constructed and tested four plausible models based on the relationship with external modes, which are presented in Fig. 6.

Isolated model: This model is composed of interactions among populations within a barrel cortical column (intrinsic connectivity only), without interaction with external modes (Fig. 6a). This model does not contain top-down modulations.

Excitatory top-down model: This model includes bidirectional interactions with an excitatory mode in the external sources (Fig. 6b).

Inhibitory top-down model: This model includes bidirectional interactions with an inhibitory mode in the external sources (Fig. 6c).

Full top-down model: The fully connected model includes connections with the excitatory and inhibitory modes in the external sources

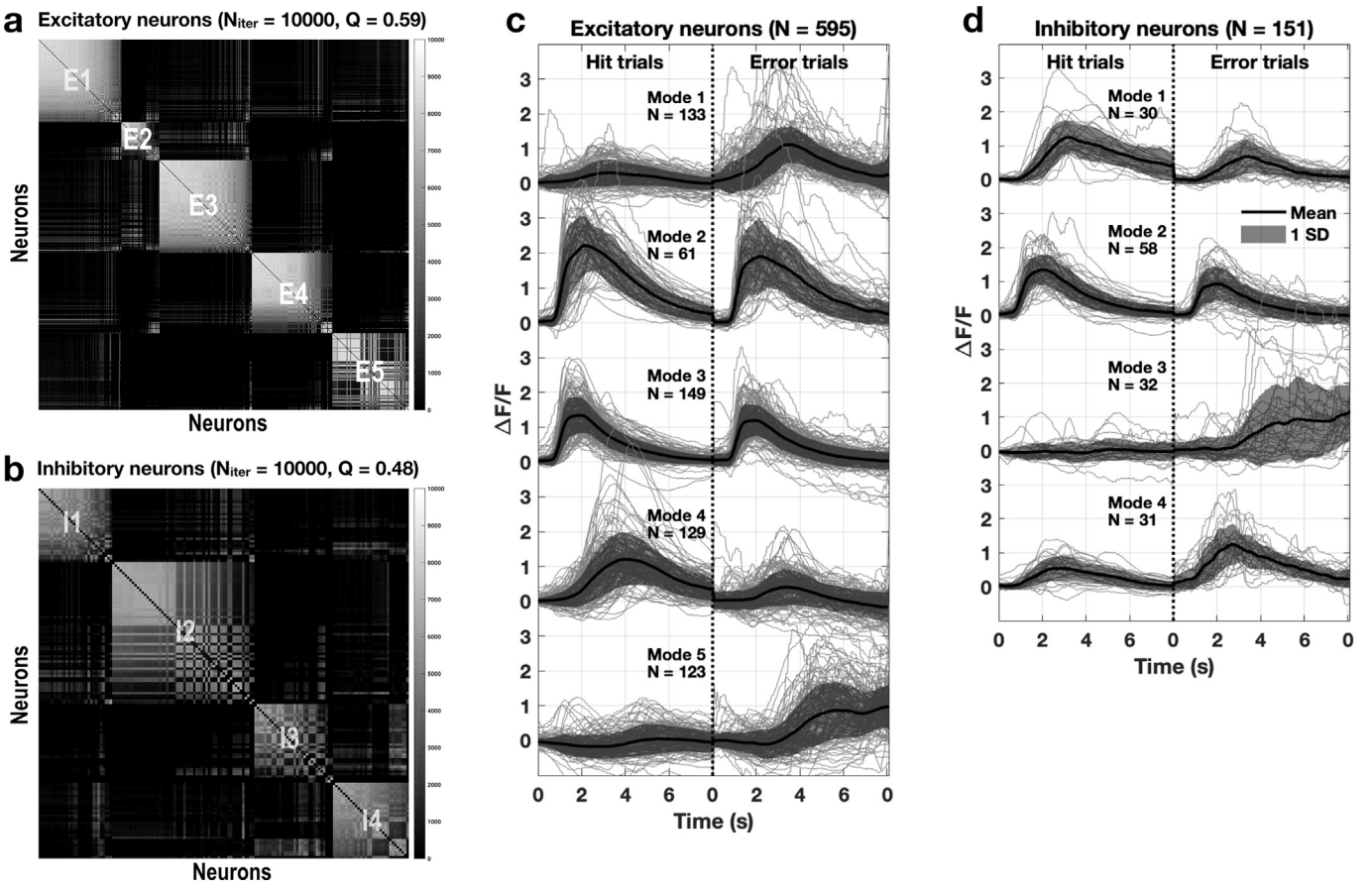

Fig. 3. Identification of neural populations. (a) and (b) display excitatory and inhibitory frequency adjacency matrices after modularity optimization. The frequency adjacency matrix indicates the frequency for each pair of neurons being a same cluster after 10000 repeated k-means clustering. The sequence of neurons was reordered according to the result of modularity optimization, which results in E1–E5 and I1–I4. (c) and (d) show evoked calcium signal traces (for hit and error trials) at the neurons corresponding to each mode (c: excitatory modes, d: inhibitory modes corresponding to E1-E5 and I1–I4 in (a) and (b)). The average trace of all evoked calcium traces corresponding to each mode is used for DCM analysis.

(Fig. 6d).

All the models consisted of four parts: six neural populations in the layer 2/3 of a barrel cortical column, the ventral posteromedial nucleus (VPM) of the thalamus, the L4, and excitatory and inhibitory external modes (E1–E3; and I1, I2, and I4). In these models, only neural populations in the layer 2/3 are observed. The L4 and two external modes (E and I) are latent states to be estimated. (Indeed, all the neural states and parameters in both the neural state model and observation model are unobserved, i.e., latent). Note that the two latent external modes may not have identifiable neural sources but rather indicate equivalent modes to elicit excitatory and inhibitory influences on the intrinsic neural connectivity in the layer 2/3. The latent states of external modes were set to be involved in the same neural dynamics as those observed in the neural populations in the layer 2/3. In other words, no specific configurations were assigned for the latent states for the external modes differently from those for the observed modes in the dynamic equation. We assigned unidirectional connections from the VPM to the L4 and from the L4 to the neural populations in the layer 2/3 as bottom-up processes. We also assumed that the inhibitory modes in the layer 2/3 do not influence the external modes.

In the current computational model, parameters corresponding to the intrinsic biological properties for the neural and the calcium dynamics were exponentiated and multiplied by reference values for the intrinsic properties adopted from previous studies. The reference values are listed in Table 1. This exponentiation makes the real effect of each parameter (with a prior of a zero mean normal distribution) positive.

Excitatory and inhibitory nodes were set to exert polarized effects (effective connectivity) on target nodes. The polarized effects were represented by the multiplication of signs (determined by presynaptic neuron types, +1 for excitatory neurons and −1 for inhibitory neurons) with (positive) exponential transformation ($\gamma_0 e^{\gamma_{nm}}$) of the connectivity parameter (γ_{nm}) with a reference value γ_0.

To select optimal reference values, we used Bayesian optimization algorithm (Shahriari et al., 2016), which is often used to search optimal hyperparameters in the machine learning. By using Bayesian optimization, we determined $\gamma_0 = 0.17$ and set the prior for the intrinsic connectivity parameter (γ_{nm}) to follow a normal distribution with zero mean and relatively high covariance (1/32). Similarly, we optimized strength $C_0 = 0.25$ of the external stimuli ($C_0 e^C$), half-activation voltage for HVA ($V_{HVA} = -27.89$), converting and scaling parameter ($\kappa_{Ca} = 0.26$), and scale parameter for the fluorescence trace ($\kappa_F = 9.85$).

DCM model inversion and model selection procedures are explained in the following sections.

2.7. Bayesian model inversion using DCM

The hidden states and parameters in both the neural state model and the calcium observation model were inferred from observed calcium signals using a standard variational Bayesian scheme under Laplace approximation (Friston et al., 2003, 2007) (spm_nlsi_GN.m in the SPM toolbox).

The variational expectation-maximization (EM) tunes a set of free model parameters θ to predict observed signals (y), by maximizing the model evidence, or model log-evidence ($ln\ p\ (y|m)$). The model log-

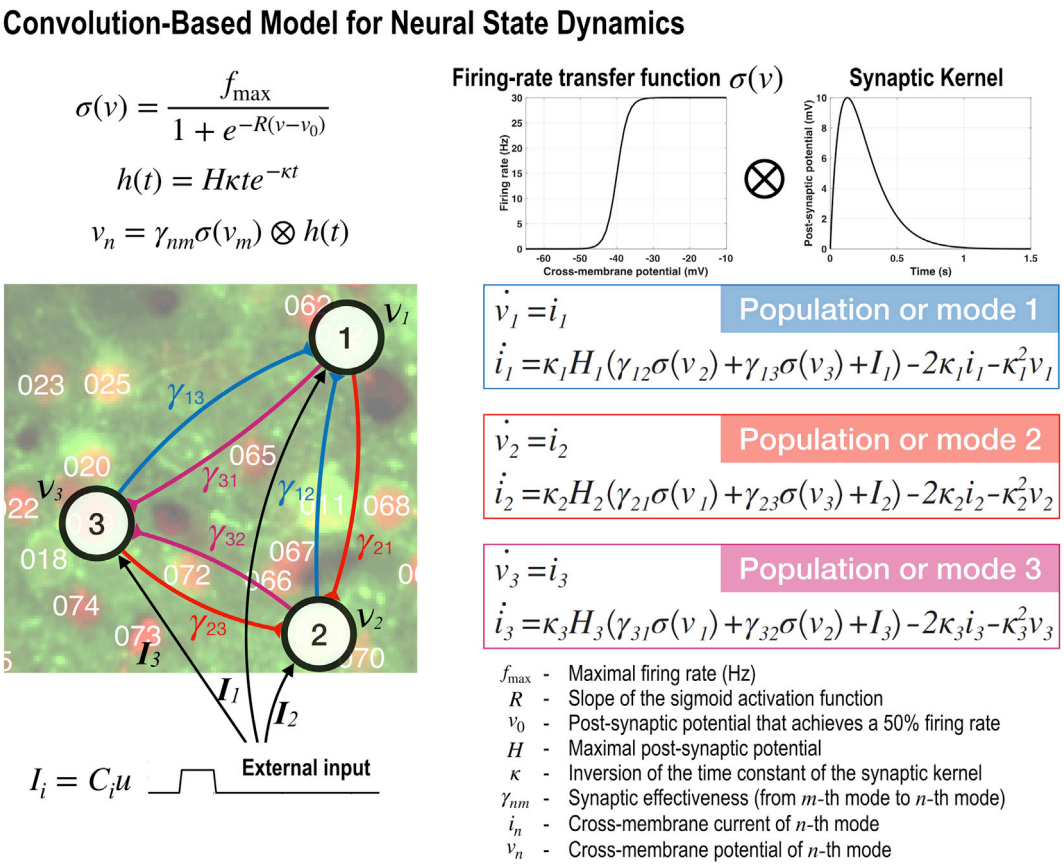

Fig. 4. A computational model for generating calcium signals at a neural circuit composed of three exemplary nodes. The equations describe the convolution-based model for the neural state dynamics. The sigmoid activation function $\sigma(v)$ stands for the relationship between the membrane potentials and the firing rates, called a firing-rate transfer function. The synaptic kernel $h(t)$ transforms the firing rate into the post-synaptic potentials. The membrane potential v_n of a post-synaptic mode is derived by convolution of the sigmoid function and synaptic kernel. The differential equation for each node is derived by the convolution of the synaptic kernel and the sigmoid activation function.

evidence can be described in terms of the free energy and KL-divergence between the posterior distribution $p(\theta|y,m)$ and its approximate distribution $q(\theta)$,

$$\ln p(y|m) = F(q,y) + KL(q(\theta)||p(\theta|y,m)) \quad [5]$$

$$F(q,y) = \int q(\theta) ln \frac{p(y,\theta)}{q(\theta)} d\theta \quad [6]$$

Since KL-divergence is non-negative, the free energy F is an approximate (lower bound) for log-evidence. The objective of optimization is to obtain an approximate distribution $q(\theta)$ that maximizes F, thus results in $q(\theta) \approx p(\theta|y,m)$. Under the Laplace approximation, the posterior moments (mean and covariance) of $q(\theta)$ are updated iteratively using an EM algorithm, which consists of expectation (E) and maximization (M) steps. In the expectation step, the conditional expectations and covariances of parameters θ are estimated by maximizing the free energy F, with given hyperparameters for error variances, using a Gauss-Newton algorithm. In the maximization step, the hyperparameters are updated in the same way to maximize free energy, based on the parameters estimated in the E-step (Friston et al., 2007). It should be noted that parameters for latent neural states corresponding to unobserved external modes and those corresponding to observed modes are both latent (unobserved) to be estimated from the data. As a function of parameters associated with observed and unobserved data, the dynamic model generates signals that correspond to observed data. The EM algorithm searches optimal parameters to minimize prediction errors between generated signals and observed data. The unobserved activity and connectivity from latent modes were estimated due to the topology of interactions among modes which imposes constraints on each nodal activity. This renders us to unravel hidden (latent) properties while coevolving circuity estimation using observed data.

2.8. Bayesian model comparison and parametric empirical Bayesian group level inference

To select the most compelling model among four models (i.e., with no external modes, only excitatory or inhibitory external mode and both excitatory and inhibitory external modes), we conducted group (between-subject)-level analysis for DCM of the four models using the parametric empirical Bayesian (PEB) scheme in SPM12.

PEB allows us to identify between-subject effects based on specified design matrices at the second level, the details of which can be found in previous studies (Friston et al., 2015, 2016). Briefly, the first-level (within-subject) effects are summarized in terms of posterior expectations and covariances, and are passed to the second-level (between--subject) to estimate posterior expectations and covariances of group means and between-subject effects. At the second level, the between-subject effects β on within-subject effects $\theta = \{A, C, \theta_h\}$ are encoded by a second-level design matrix X (Eq. (7) and Eq. (8)).

$$y_i = \Gamma(\theta_i) + \varepsilon_i^{(1)} \quad [7]$$

$$\theta = X\beta + \varepsilon^{(2)} \quad [8]$$

Here, Γ is a function that returns the predicted observations as a function of model parameters (corresponding to Eq. (1) and Eq. (2) for the neural state model, and Eq. (3) and Eq. (4) for the observation

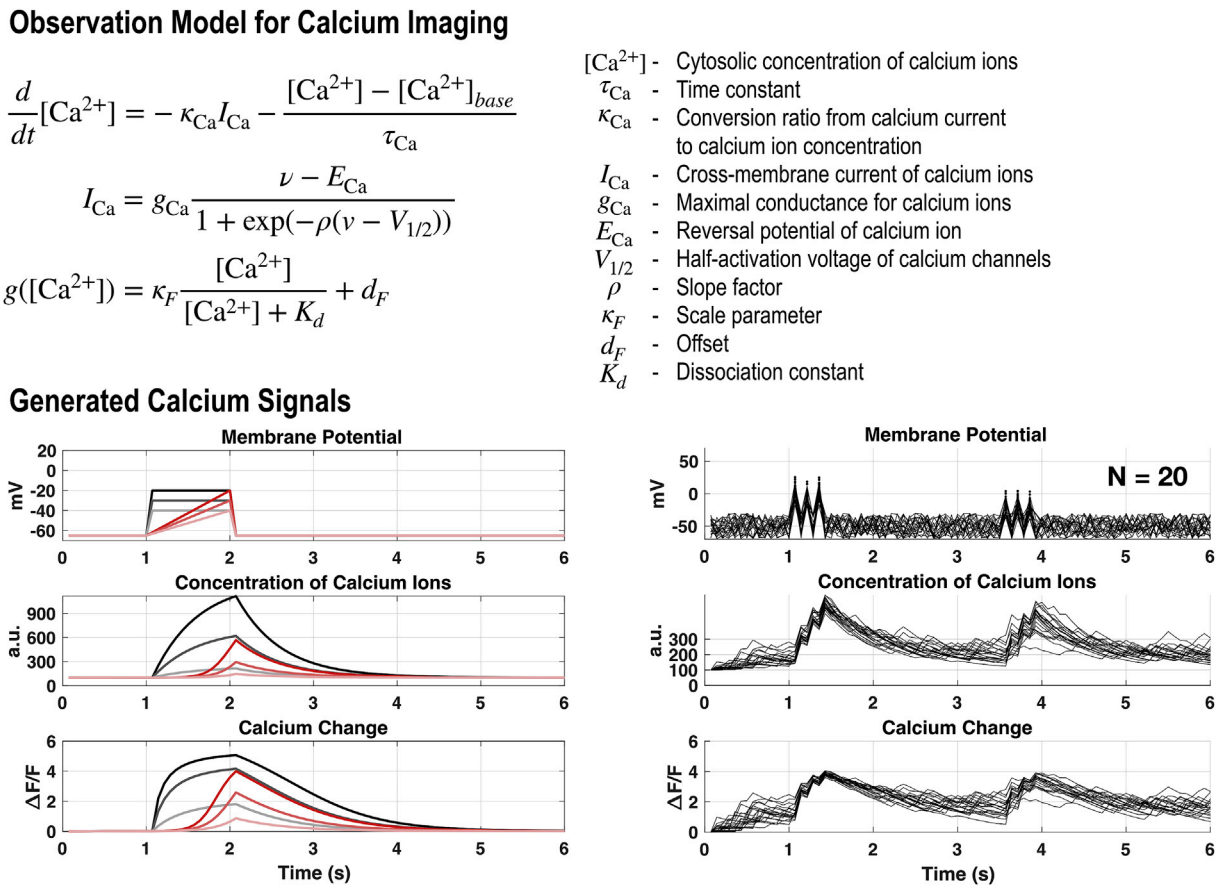

Fig. 5. An observation model for calcium signals and its simulation examples. The top shows the equations for describing calcium dynamics, with descriptions of the parameters used. The bottom shows the results of two simulations using the observation model for calcium imaging. The bottom left panel displays the changes in the concentration of calcium ions and corresponding signals ($\Delta F/F$) due to simple changes in the membrane potential while the right panel presents those for more complex changes in the membrane potential, with a background noise (N = 20).

model). The hierarchical or PEB model indicates that the parameters θ_i of the ith subject are modeled as the sum of the group level prediction $X\beta$ and a random effect $\varepsilon^{(2)}$.

In the current study, we used a design matrix X of seven regressors, which is composed of a group common (a vector of ones), a group (condition, hit vs. error) difference (a vector of $[1\ 1\ \ldots\ 1\ {-1}\ {-1}\ \ldots\ {-1}]^t$, and five hit-error pairs of five mice to explain within-subject effects (Fig. 8).

We selected the best model by evaluating free energy (approximated log model evidences) of the group-level model (PEB) for each set of DCM estimates for the four models, described above.

2.9. Bayesian model reduction

We performed Bayesian model reduction (BMR) (Friston and Penny, 2011) from the group level model estimate (PEB) of the best model using *spm_dcm_peb_bmc.m* in SPM12. BMR reduces a model by testing the redundancy of each parameter (or a set of parameters, mostly edges) in the model by comparing the free energy (an approximated log model evidence) of the reduced model (after shrinking the parameter) with that of the full model. If the free energy for the reduced model does not decrease compared to the model before shrinking, the parameter is considered to be redundant, and is removed from the full model.

To search the best combination of redundant edges to remove from the full model, we performed a greedy search algorithm (Friston and Penny, 2011). Note that the shrinking strategy differs for group common effects and group difference effects (β) specified in the first and second design matrix X in Eq. (8). For group common effects (β corresponding to the first column of X), we set -4 as an expectation and 0 as a covariance of the prior to shrink the parameter to make the real effects (mostly, connectivity) very small after exponential transformation, i.e., exp (-4). To shrink group difference effects (β corresponding to the second column of X), we assigned zeros for both the expectation and covariance of the prior for each effect (parameter for group difference) in the reduced model. The Bayesian model average (Penny et al., 2010) performed on the models from the last iteration of the greedy search algorithm was used for subsequent analysis and interpretation (Fig. 8).

3. Results

3.1. Selection of neural populations via wave-sorting

The calcium signals of 595 excitatory and 151 inhibitory neurons in the layer 2/3 of the barrel cortex of five mice were sorted into multiple modes. The percentage ratio of inhibitory neurons to neurons in the layer 2 of a barrel column is 20.2%, which is similar to that of Meyer et al. (2011) (20.8%).

When the modularity-optimizing process was applied (see Fig. 1), the modularity Q of excitatory (five modes) and inhibitory (four modes) clusters were 0.48 and 0.40, respectively (Fig. 3a and b), which indicate a strong community structure, and thus, a strong consensus across k-means clustering experiments (Newman and Girvan, 2004). We found five modules for excitatory neurons and four modules for inhibitory neurons (Fig. 3).

Since the purpose of the current application was to show the usefulness of DCM for CaI by analyzing a relatively simple contrast for neural connectivity, responding to hit and error trials at the early stage of sensory

Table 1
Parameters used in the computational model constructed for dynamic causal modeling of calcium signal.

Parameter	Variable	Type	Value[a]	Unit	Reference
Neural state model					
Connectivity[b]	γ_{nm}	Unfixed	(0)	–	
Connectivity reference[c,d]	γ_0	Fixed	0.17	–	
Connectivity from input stimuli[b]	C	Unfixed	(0)		
Reference connectivity from input stimuli[c,d]	C_0	Fixed	0.25		
PSP that achieves a 50% firing rate of a neural population[e]	V_0	Fixed	−40	mV	
Inversion of time constant of the kernel of PSP	K	Unfixed	[7.81]	s^{-1}	Yaksi and Friedrich, 2006
Maximal PSP	H	Fixed	27.18	mV	
Slope of the sigmoid activation function[e]	R	Fixed	0.67	mV^{-1}	Moran et al. (2013)
Maximal firing rate[e]	f_{max}	Fixed	30	Hz	
Observation model (Calcium ion channels)					
Half-activation voltage for HVA[d]	V_{HVA}	Fixed	−27.89	mV	Lee (2013)
Slope of the sigmoid activation function	ρ	Fixed	0.2	mV^{-1}	Rahmati et al. (2016)
Time constant of the kernel of calcium	τ_{Ca}	Unfixed	[0.8]	s	Rahmati et al. (2016)
Converting and scaling parameter[d]	κ_{Ca}	Unfixed	[0.26]	–	
Maximal conductance for calcium ions	g_{Ca}	Fixed	5	mS/cm[b]	Rahmati et al. (2016)
Scale parameter for the fluorescence trace[d]	κ_F	Fixed	9.85	–	Yaksi and Friedrich, 2006
Offset parameter for the fluorescence trace	d_F	Fixed	−3.28	–	(calibrated)
Baseline calcium ion concentration	$[Ca^{2+}]_{base}$	Fixed	100	nM	Rahmati et al. (2016)
Dissociation coefficient	K_d	Fixed	200	nM	Rahmati et al. (2016)

HVA: High voltage-activated calcium channel, PSP: post-synaptic potential.
[a] Values in parentheses (.) and brackets [.] were used as prior expectation and reference values for parameter estimation.
[b] Covariances of connectivity were 1/32. Covariances of the other parameters were 1/256.
[c] Connectivity reference is used for exponential transformation of connectivity parameters (γ_{nm}) to make effective connectivity ($\gamma_0 e^{\gamma_{nm}}$) positive. The other reference values for unfixed parameters were similarly used for exponential transformation.
[d] Bayesian optimization method was employed to adjust parameters which were considered as hyperparameters.
[e] Refer to Discussion section for the selection of those values.

processing, we excluded the excitatory mode 4 (E4) and mode 5 (E5) and the inhibitory mode 3 (I3) due to their delayed peaks (~4 s). Although E4 showed a relatively clear response to the first touch, calcium responses with delayed peaks for hit trials might contain reward processing rather than the early sensory processing (The reward was given at 2.6 s after the target pole appeared for hit trials and calcium signals respond approximately 0.8 s later according to the start time for CaI rising in E2 and E3 of Fig. 3c). Considering that the sensory processing at the later stage may recruit a neural connectivity different from that of the early stage processing, we excluded E4 in the subsequent modeling of the early stage processing. Finally, six modes (three excitatory and three inhibitory) were included for the computational modeling of the layer 2/3.

3.2. Model parameters for calcium imaging

To make the models realistic, we used a set of fixed parameters for neural state and calcium signal dynamics based on previous studies (Gentet et al., 2010; Lee, 2013; Moran et al., 2013; Rahmati et al., 2016; Yaksi and Friedrich, 2006). The parameters used in this study are listed in Table 1. The unfixed model parameters were estimated using the expectation-maximization process in DCM, with the parenthesized values in Table 1 as reference values. During the pre-stimulus period of each trial (zero CaI), the negative offset parameter (d_F in Eq. (4)) for the fluorescence trace equals the signal change term of Eq. (4), $\kappa_F[Ca^{2+}]/([Ca^{2+} + K_d])$. Therefore, the value of the offset parameter was computed by using the scale parameter, baseline concentration, and dissociation constant.

3.3. A simulation study of the computational model

To test the validity of DCM for CaI data, we conducted a simulation study with a simplified model topology but similar (or same) intrinsic properties used in the experimental study (Fig. 6d). We established a ground truth model with a pre-specified connectivity and parameters (Fig. 7a), and generated membrane potentials and CaI signal changes in each neuron according to the dynamic neural state and observation equations (Fig. 7b).

For the generated CaI signals, we specified a model with an intrinsic connectivity identical to the true model, and applied model inversion using DCM. Membrane potentials and calcium signals for all neurons (E1, E2, E3, and I1) assessed using the estimated parameters are displayed in Fig. 7c (dotted lines) with simulated signals (solid lines). It reliably estimated parameters of the specified model with high reliability (Fig. 7d and e). For a noisy time series (a simulated signal added with a Gaussian noise with mean 0 and standard deviation of 0.15) and with a hidden node, DCM for CaI estimated the model parameters within a reasonable range (Fig. 7f, g, and 7h).

Since a prior knowledge for the connectivity topology is not generally available, we constructed 255 models with all possible model topologies, reduced from the full model where all nodes (E2, E3, and I1) are fully connected with each other (Fig. 7l). For reduced models, we estimated parameters and free energy of each model using DCM (Fig. 7m). The best model (with the highest free energy) had an identical topology and very similar parameters with those of the true model (Fig. 7i, j and 7k).

3.4. Bayesian model comparison in the experimental data

The free-energies of PEB for the four models, evaluated to find the most reliable model among four models for the real CaI data set, are −37917.3, −25691.4, −26119.9 and −802.1. The result suggests that the model with both excitatory and inhibitory external modes (model 4) was found to be the best for describing CaI signals in the barrel cortical column.

3.5. Effective connectivity for different types of trials

The common and different effective neural connections between hit and error trials were evaluated using a group-level PEB, followed by Bayesian model reduction (using a greedy search algorithm) and Bayesian model average (Fig. 8). Fig. 8a and c shows a circuit with common effective connectivity for hit and error trials. For both hit and error trials, there were bottom-up (from L4) and top-down (from external sources) connections with the modes in the layer 2/3 of the barrel cortical column. The bottom-up excitatory L4 affects mainly E2, E3, and I2. The excitatory external mode modulates E3 and I1, and the inhibitory external mode inhibits E3 and I2. Both external modes receive inputs primarily from E2.

The difference in the effective connectivity for hit and error trials is

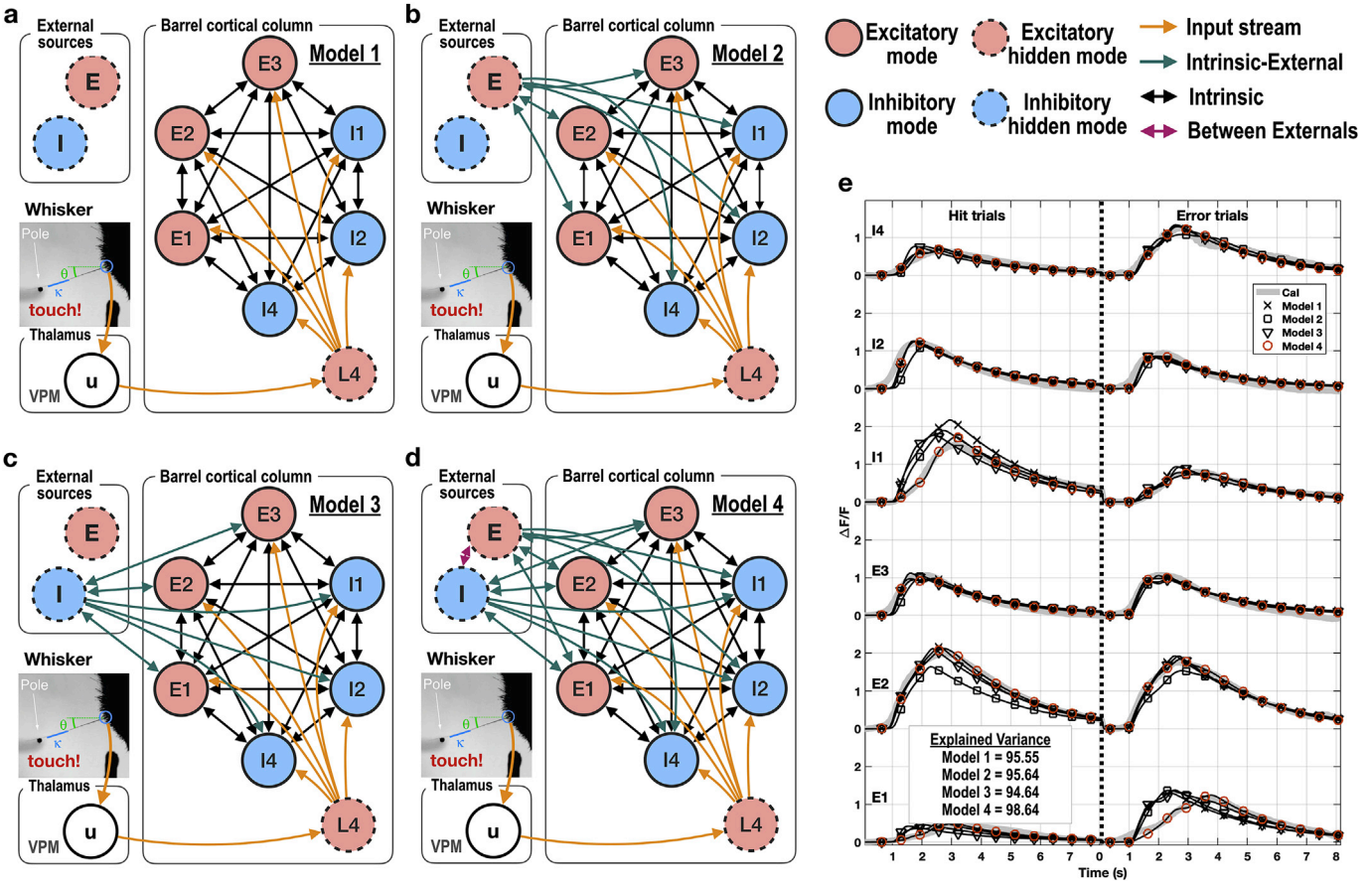

Fig. 6. Four models for the barrel cortical column used in the current study. (a) Model 1 is composed of interactions among six modes in the barrel cortex without interactions with external modes (isolated model). (b) Model 2 considers a latent excitatory external mode for hierarchical interaction. (c) Model 3 considers a latent inhibitory external mode. (d) Model 4 has two latent modes, as a fully connected model (excitatory and inhibitory top-down modulation). (e) As an example of model estimation, observed and estimated CaI signals of a mouse using four different models are presented in thick gray lines and marker lines. Red-circled signals are the result of the model 4 (the best model). The group-level free-energies are −37917.3, −25691.4, −26119.9 and −802.1.

shown in Fig. 8b and d. During hit trials, the latent excitatory L4 influences E1, E3 and I4 less than during error trials. The interactions with the external modes are more active during hit trials than error trials. In particular, the external excitatory mode excites I2 more but E2 less, receives increased input from E2 and E3 during the hit trials than the error trials. The inhibitory external mode inhibits E1 more but less E3 and I1 during the hit trials. The increased latent input from L4 increases the activity of I4, E1 and E3 more during error trials than during hit trials. During the error trials, the within-columnar interactions increase compared to during the hit trials. The computational model suggests that processing of hit and error trials recruits different level of intrinsic connectivity of the layer 2/3 in the barrel cortical column in connection with external modes.

4. Discussion

In this study, we proposed a computational scheme for analyzing neural interactions reflected in the CaI under a DCM framework by combining neural state and calcium ion concentration dynamic models. Since changes in cytosolic concentration of calcium ions reflect post-synaptic neural activity (Berger et al., 2007) (i.e., calcium signal indicates the discharge of post-synaptic action potentials), it is advantageous for evaluating causal relationships or effective connectivity among neurons or neural populations using CaI signals. To model effective connectivity using CaI data, we combined a neural state dynamic model and CaI observation model following the general framework of DCM. Using this method, we evaluated intrinsic and extrinsic effective connectivity between neural populations in a barrel cortical column differentially responding to hit and error trials. Using the current computational model, we showed that the external signals outside the barrel cortical column play an important role in explaining hit- and error-related neural activity within the column.

4.1. Neural state dynamic model for neural population activity

Previous studies have shown that neurons in the brain encode and process information as populations rather than individually (Pasupathy and Connor, 2002; Pouget et al., 2000). This principle of population coding (or rate coding) provides a theoretical basis for developing a microcircuit or brain-like system in a practically accessible manner (Bastos et al., 2012; Mizrahi et al., 2018). In this type of neural population (or ensemble) coding approach, neurons in the population are assumed to share the same neural state and are not distinguishable from each other in terms of activity (Deco et al., 2008; Knight, 1972).

For the neural state dynamic model of ensemble activity, we used a convolution-based model which comprises inter-modal connectivity with an activation function from pre-synaptic membrane potential to firing rate for each population and a synaptic kernel mapping from the firing rate to post-synaptic membrane potential (Marreiros et al., 2008; Moran et al., 2013). Since the convolution-based neural state model focuses on the probabilistic information transfer between neural populations, the ensemble activity of neurons is generally described by the mean property of neurons in the population. Therefore, the firing-rate transfer function converts presynaptic mean membrane potential to mean firing rate of a

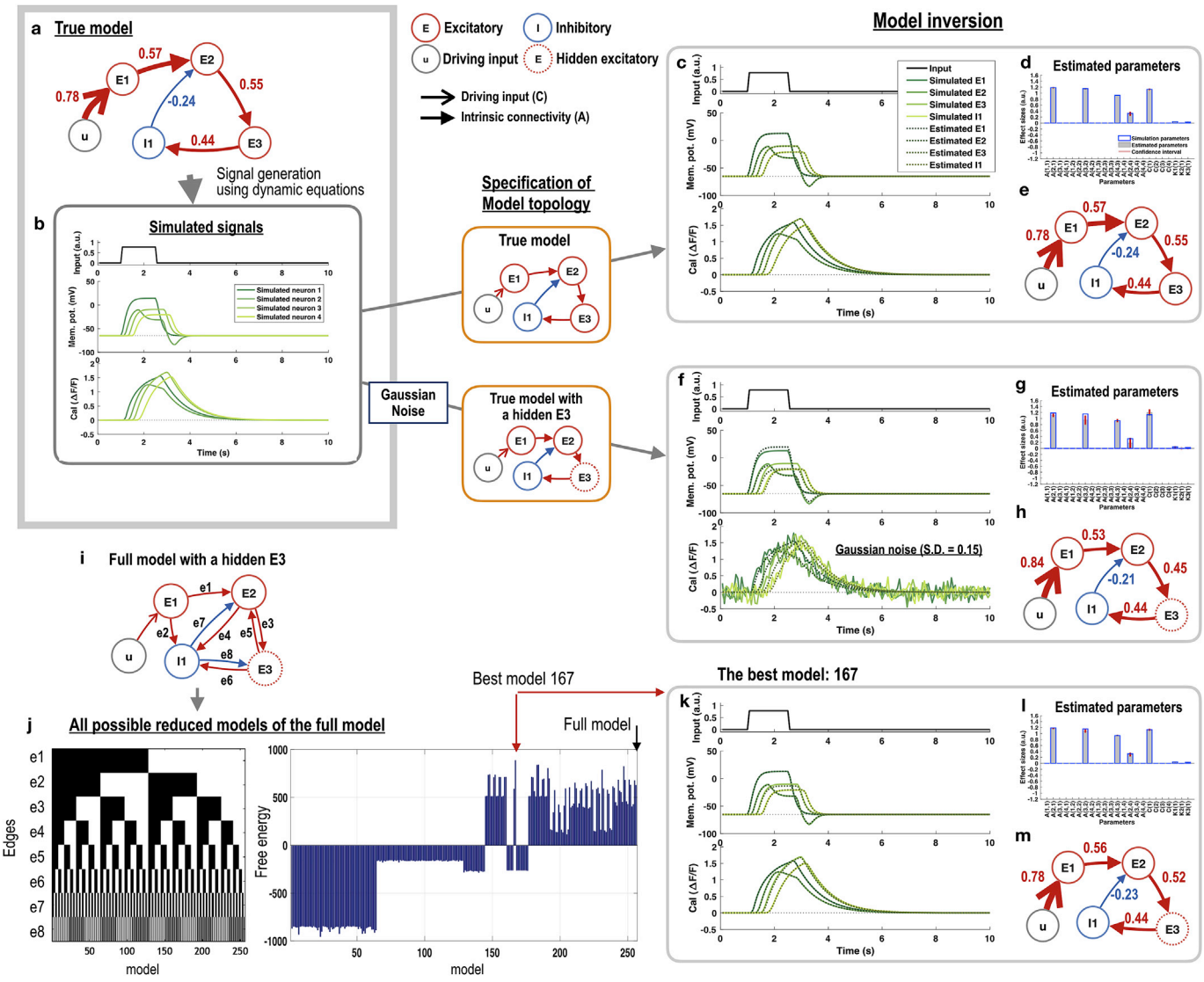

Fig. 7. A simulation study of computational models for calcium signals. (a) A true model is shown. (b) Membrane potentials (middle panel) and calcium signals (bottom panel) at each node are generated by driving input u (top panel) using the true model specified in (a) and Eqs. (1)–(4). The E1 node (corresponding to the L4 in Fig. 6) converts the driving input u to biologically plausible input to E2 (and I1 in i). The estimated model parameters and estimated signals are presented for two model specifications; (c–e) using the specified true model topology and (f–h) using the specified true model topology but assigning E3 as a hidden node (not using the E3 signal in the model inversion) for signals with a Gaussian noise (with zero mean and standard deviation of 0.15). From the full model (fully connected among E2, E3 and I1) with a hidden node E3 (i), all possible reduced models are generated by switching each edge (e1 ~ e8) on and off (the left panel of j). Free energies for all possible 255 models after DCM inversion are presented (the right panel of j). The 167th model shows the highest free energy and is chosen as the best model. The best model appears to have the exact topology of the true model, which is presented in (k–m). In all models, we assigned driving input u only to E1, scaled by the C matrix via $C_0 \cdot e^C$. For each model inversion, simulated (solid lines) and estimated (dotted lines) membrane potentials (middle panel) and calcium signals (bottom panel) for each node are presented (c, f, and k). In (d, g and l), the expectation (blue edged bar) and 95% credible interval (red bar) for each parameter in each model, and the true parameter values are shown. A indicates effective connectivity (γ_{nm}) among (E1, E2, E3, and I1). The three unfixed parameters (K1, K2, and K3) represent deviations from intrinsic properties of a node, such as the inversion of time constant of the kernel of postsynaptic potential (κe^{K1}), the converting and scaling parameter ($\kappa_{Ca} e^{K2}$), and the time constant of the kernel of calcium ($\tau_{Ca} e^{K3}$) using reference values of κ, κ_{Ca}, and τ_{Ca} in Table 1.

local population (Liley et al., 2009; Marreiros et al., 2008, 2010; Spiegler et al., 2010). The mean postsynaptic potential is calculated in terms of convolution of a synaptic kernel with the mean firing rate of a neural population (called "neural mass") (Freeman, 1975; Jack et al., 1975; Jansen and Rit, 1995; Wilson and Cowan, 1972). In practice, it is not easy to determine reference values for the parameters of the firing-rate transfer function ($\sigma(v)$ in Eq. (1)), such as the post-synaptic potential V_0, maximal firing rate (f_{max}) and slope of the sigmoid activation function (R), presented in Table 1 and Fig. 4. The firing-rate transfer function for a population can be described as a combination of a population dynamics function (how many neurons in a population are activated) and a neuron-specific firing rate function (how many times a neuron fires per a second) of different membrane potentials. Since references for a neuron-specific firing rate function are rarely available (indeed, derivation of a post-synaptic potential that achieves a 50% firing rate in a neuron is difficult in the electrophysiological experiments), we simplified the firing-rate transfer function to follow mostly the function of population dynamics. Since the action potential threshold is around −40 mV in the barrel cortex L2/3 (Gentet et al., 2010; House et al., 2011), a Gaussian cumulative distribution function (with a center at −40 mV) can be used to describe the proportion of the firing neurons in the population. However, we used a sigmoidal function with a center at −40 mV to allow slightly wider dynamic range (monotonic increase) than Gaussian cumulative distribution function for the given slope R = 0.67. Nevertheless,

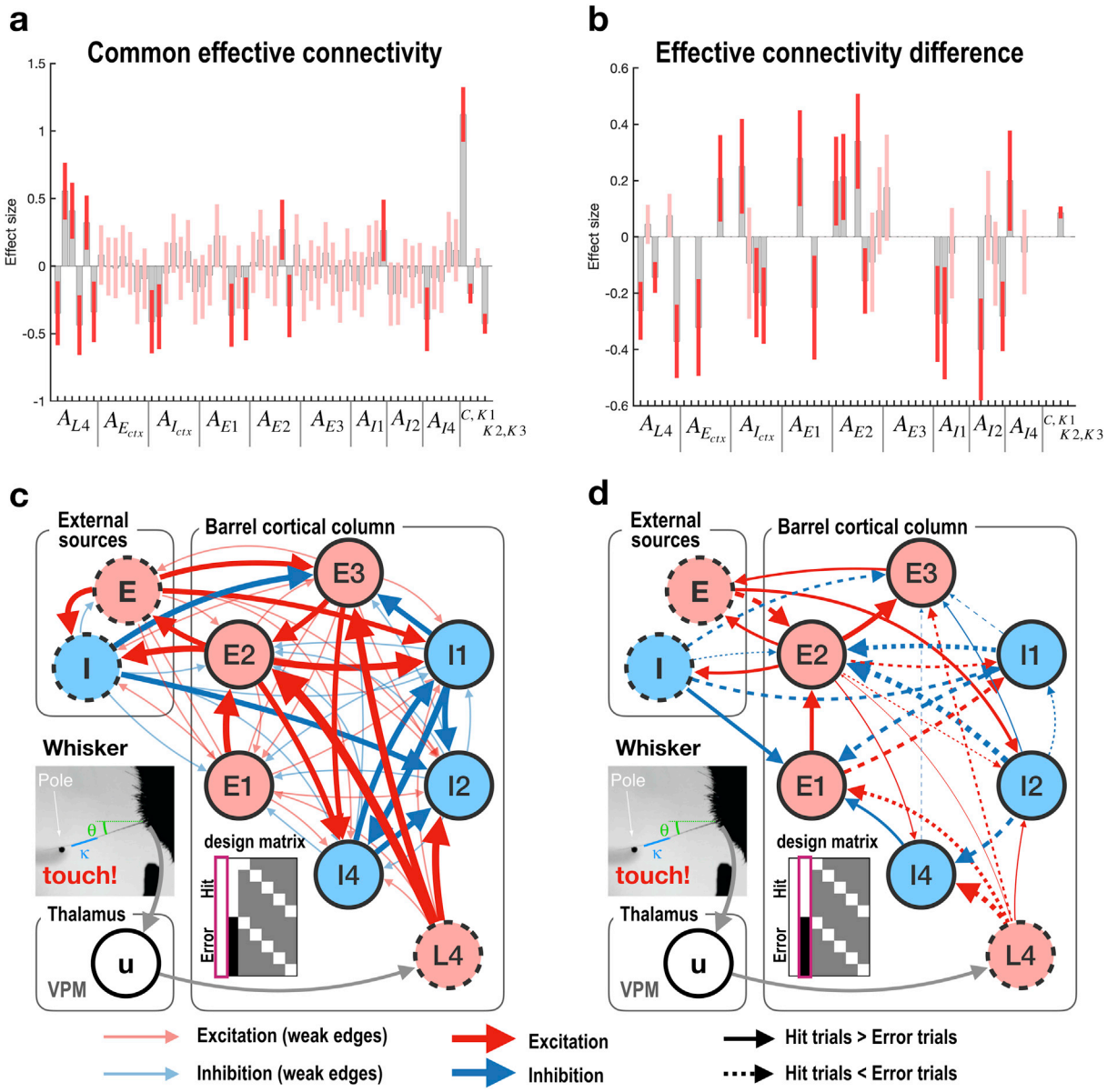

Fig. 8. Results obtained using parametric empirical Bayesian scheme for assessing common and different effective connectivity between hit and error trials. In (a) and (b), subdivisions in the x-label (e.g., A_{L4}, A_{Ectx} and so on) indicate connectivity from the labeled modes (for example, A_{L4}, connectivity from L4 to other modes). The input stimulus is scaled by the C via $C_0 \cdot e^C$. The K1, K2, and K3 modulate the inversion of time constant of the kernel of postsynaptic potential (κe^{K1}), the converting and scaling parameter ($\kappa_{Ca} e^{K2}$), and the time constant of the kernel of calcium ($\tau_{Ca} e^{K3}$) using reference values of κ, κ_{Ca}, and τ_{Ca} in Table 1. The red bars indicate 95% confidence intervals around the posterior estimates (gray bars). (a) and (c) show the common effective connectivity between two types of trials (hit and error conditions). It corresponds to the first column (constant) of the design matrix X in Eq. (8). (b) and (d) display differences in the effective connectivity between hit and error trials (condition difference) after Bayesian model reduction using a greedy search algorithm. It corresponds to the second column (hit minus error) of the design matrix. In (a), the red bars indicate that the γ_{nm} differs significantly from γ_0 in Table 1 (rather than no connection or zero connectivity). Thick and thin lines indicate that the common connectivity is higher or lower than the reference value γ_0. In (b), the red bars display connectivity changes due to different trials that survived a non-zero criterion with a posterior confidence of 95%. In (c) and (d), circles with red and blue colors indicate excitatory or inhibitory nodes. Lines with red and blue colors denote effective connectivity from the excitatory and inhibitory modes. Solid and dotted lines in (d) indicate increased and decreased connectivity, respectively, in the hit trials compared with the error trials. Only the difference in K2 shows non-zero with a posterior confidence of 95% but did not pass the Wilcoxson sign rank test for hit and error trials ($p > 0.05$).

we acknowledge that this is not an optimal solution but should be researched in the future study.

Note that the mean membrane potential in the current model (Eqs. (1) and (2)) above the expected actional potential threshold may reflect a mean depolarization envelop of the neurons in a population (Antic et al., 2016). In the simulation (Fig. 7), however, voltages at certain regions rise higher than the plateau depolarization level of depolarization envelopes (around −40 mV in Antic et al. (2016)). To resolve this problem, the simulated or inferred voltages may need to be further scaled to match the biological ranges of depolarization envelops.

In the present study, we applied DCM to CaI after averaging trials for each condition (i.e., hit or error). The difference between them was modeled in the second level design matrix using PEB. However, it is also possible to apply DCM-CaI to trial-by-trial analysis of CaI by modeling the hit and error differences using a modulation effect matrix (such as B matrix in conventional DCM). If so, it would be advantageous to constrain some parameters shared across behavioral conditions. The application and evaluation of advantages and disadvantages of trial-by-

trial analysis using DCM-CaI remains to be further researched.

Although the current DCM scheme for CaI was applied to neural populations, it can be extended to estimate interactions among individual neurons with appropriate assumptions, for example, the sigmoidal relationship between the membrane potential and the firing rate at a neuron from the stochastic neural firing perspective (Fischer et al., 2009). Alternatively, we may extend the DCM-CaI to a single neuron level by adopting spiking models (e.g., Quadratic-Gaussian Integrate-and-Fire model) in Rahmati et al. (2016), who conducted CaI modeling in the neuronal level. The practical application of DCM for CaI to a neuron level activity may require in-depth research and validation.

4.2. Observation model for calcium ion dynamics

For modeling CaI signals, we adopted a model of calcium dynamics to formulate the cross-membrane calcium current gated by the cross-membrane potential (voltage-gated calcium channels) and a model for the kinetics of cytosolic concentration of calcium ions (Rahmati et al., 2016). This differs from the convolution-based approach used by (Rosch et al., 2018), who applied an exponential decay kernel (with the parameters of GCaMP6f obtained from the study by (Chen et al., 2013)) to local field potential reflected in the calcium signals for the analysis of seizure activity.

Among multiple types of voltage-activated calcium channels (Lee, 2013), we included only a high-voltage-activated calcium channel to the current calcium dynamic model for the following reasons. First, the observed calcium signals (fluorescence transients), and specifically from the somata, are mainly due to the calcium currents of high-voltage-activated calcium channels during spiking activities (Rahmati et al., 2016). Second, adding other types of calcium channels can increase the complexity of the inversion process and thus decrease the inference accuracy.

We configured all unfixed parameters for the observation model for CaI with a high precision so that changes in the CaI between hit and error conditions are primarily attributable to the connectivity differences. When we tested the differences of the unfixed parameters for the observation model (i.e., K2 and K3, that are related to converting and scaling parameter ($\kappa_{Ca}e^{K2}$), and the time constant of the kernel of calcium ($\tau_{Ca}e^{K3}$)) across conditions using Wilcoxon signed-rank test, we found no significant statistical differences ($p > 0.05$) (however, difference in K2 was non-zero with a 95% posterior confidence).

Note that the computational model we proposed includes parameters for the kinetics of calcium signals that differ according to calcium indicators. For example, GCaMP6s used for CaI in the current study shows not only higher sensitivity (approximately sevenfold) but also has a nearly twice rise time (time-to-peak) and nearly threefold slower decay time than GCaMP6f used by (Chen et al., 2013). Thus, we used a longer time constant for the kinetics of calcium signal than that of GCaMP6f.

4.3. Bayesian model inversion in DCM for CaI

In the simulation, the proposed DCM for CaI estimated latent neural states and effective connectivity within a reasonable range from CaI data. The simulation experiment suggests that more prior knowledge regarding the circuitry or model parameters leads to more reliable estimation results (Fig. 7c, d, and 7e). However, in practice, we often lack prior knowledge regarding the system configuration. In such cases, we can use Bayesian model comparison to select the best model in explaining the observed data. We may begin our approach using a fully connected model without prior knowledge of the connectivity among nodes. The fully connected model can be compared with reduced models in terms of accuracy and complexity (the number of parameters), termed free energy (Friston et al., 2016).

We often need to estimate connectivity of the whole system using partially observed data. In the present study, from the simulation experiment, we confirmed that DCM inferred neural states and connectivity with hidden unobserved nodes (Fig. 7h). The fact that neurons or neural populations do not work in isolation but interact via a certain connection imposes constraints on each nodal activity. This compels us to unravel hidden (latent) nodal activity and connectivity while coevolving circuity estimation using observed data.

It should be noted that the optimization process in DCM estimated some effective connectivity that were absent in the true model. It is possible that the estimated parameters in the best model are not a unique solution for describing the observed data (Van Geit et al., 2016). A multitude of different configurations of circuits can generate the same activity, which is often termed degeneracy of neural systems (Edelman and Gally, 2001). In this case, model complexity matters in the selection of the best model, according to Occam's razor theory (Sober, 1990).

Besides the degeneracy problem, optimization using variational EM under Laplacian approximation is not free from the local optimum problem. The performance for optimization of nonlinear models generally depends on initial values or the prior probability. To minimize the initial value problem, we used biologically plausible reference values for intrinsic properties of neural and calcium dynamics, adopted from previous literatures. These reference values reduce the solution space of the model inversion to be biologically plausible. Various efforts to reduce the initial value problem has been conducted to reliably estimate model parameters, for example, model inversion with the prior derived from group level posterior (using PEB) (Friston et al., 2016). In the current study, we adopted only the reference value scheme, leaving evaluation of various optimization schemes for a future study. Therefore, the current results should be interpreted in consideration of the potential limitations of the model optimization process.

4.4. Latent states for intermingled modulation by other regions

In the current study, the calcium signals evoked in a multitude of neurons in the layer 2/3 of a barrel cortical column were sorted and clustered into six neural populations. The differentiation of six neural populations within the barrel column was based on their neural activity pattern for external inputs. Thus, this approach does not differentiate the interconnection among neurons or consider neural diversity within the same population, but abstracts them as a functionally homogeneous node. This sort of abstraction is advantageous as well as disadvantageous: advantageous in terms of simplifying the model and making computational modeling accessible for addressing population-level questions, disadvantageous in terms of explaining neurobiological properties and connectivity among neurons.

According to a study on neuronal morphologies of the layer 2/3 and L4 within a barrel cortical column by Petersen and Sakmann (2001), the excitatory neurons of the layer 2/3 have dense dendrites at the same layer and axonal arborizations to lateral columns and a deep layer (layer 5). Excitatory neurons of the L4 also have dense dendrites at the same layer and axons forming an ascending column of input to the layer 2/3 pyramidal neurons. Based on these findings, we constructed the current model for the layer 2/3 in a barrel cortical column that includes a hidden node corresponding to the L4. The hidden-node L4 is required to generate neural activity of spiny-stellate cells in the same layer of a barrel cortical column. Considering that sensation is delivered to a barrel cortical column via a thalamocortical pathway, we designed the bottom-up pathway, VPM-L4-layer 2/3 (Fig. 6, yellow arrows).

Touching a whisker evokes receptive neural activity in a specific column of the barrel cortex. This specificity allows the functional mapping of a target whisker (such as the directional preference map) in the layer 2/3 of a barrel cortical column (Andermann and Moore, 2006). Despite columnar specificity of whiskers, the neural population in a column of the barrel cortex does not only process bottom-up signals but also integrates information from (or modulated by) neighboring columns (Petersen and Sakmann, 2001) and/or other external brain sources (Manita et al., 2015; Zagha et al., 2013). Therefore, we introduced latent

excitatory and inhibitory modes for external sources outside the model of a barrel cortical column. It has long been debated whether external input to a cortical column is inhibitory or excitatory (Wang et al., 2013; Wang, 2002; Zagha et al., 2016). The current computational model suggests the need of both types of external sources (the model 4 in Fig. 6). The two external sources represent mixtures of all possible external effects on the column of the barrel cortex. A cortical column in the barrel cortex receives/sends neural signals through long-range projections from the contralateral (Petreanu et al., 2007) and ipsilateral (Kinnischtzke et al., 2014; Manita et al., 2015; Petreanu et al., 2012) cortices. It should be noted that both long-range excitatory or inhibitory projections from external sources can exert inhibitory modulations to a cortical column. The long-range excitatory projection can evoke inhibitory interneurons to inhibit the other neurons in the same column (Aronoff et al., 2010). Furthermore, neurons in a column can be directly modulated by the long-range inhibitory projections (Tamamaki and Tomioka, 2010). These two types of inhibitory modulations may explain the difference in the effective connectivity for hit and error trials in Fig. 8d. In addition to long-range projections, we cannot rule out the possibility that the connections with external modes represent lateral connection with neighboring columns in the barrel or motor cortices. The details of the types of external sources and interconnections with them remain to be explored using more experimental data.

According to a recent canonical microcircuit constructed based on the framework of hierarchical predictive coding (Bastos et al., 2012), the supragranular layer (layer 2/3) interacts with hierarchically higher regions by receiving descending predictions from and sending ascending prediction errors to the higher regions. In this perspective, the external sources may play critical roles that regulate the neural populations at the layer 2/3 within a barrel cortical column.

The role of reciprocal interaction between the external sources and the intrinsic effective connectivity in the layer 2/3 has been studied previously. Manita et al. (2015), for example, showed that the somatosensory cortex (S1) and secondary motor area (M2) form a top-down circuitry to perceive tactile stimulation. The study revealed that sensory stimulation induces neural activity sequentially from the S1 to the M2, followed by the M2 to the S1 in a reverse sequence. The reciprocal signal processing is similar to the processing of the best model in the current study (Fig. 8). Moreover, the degradation of sensory perception after inhibition of the axons projecting from the M2 to the S1, reported in (Manita et al., 2015), is consistent with the current result of (strongly) decreased inhibitory effects from the external modes during error trials compared to hit trials. As shown in Fig. 8d, the external inhibitory mode disinhibits (or inhibits less) the intrinsic E1 and the external excitatory mode excites less the intrinsic I2 mode during error trials than during hit trials.

The gross difference in the connectivity between hit and error trials can be characterized by redistribution of connectivity. In the processing of hit trials, interactions between the intrinsic neural modes at the layer 2/3 and external modes increase compared to those of error trials (Fig. 8). In particular, the external sources receive increased signals from the neural modes in the layer 2/3. Meanwhile, increases in the interactions among the modes within the layer 2/3 are dominant during error trials, particularly from the inhibitory modes. Despite different behavioral responses, the connectivity does not exclusively increase or exclusively decrease for hit trials compared to error trials. The functional circuitry seems to work in balance. For example, E1 has more effects on E2 but E1 itself is more suppressed by I4 and external I as well as reduced input from L4 during hit trials than during error trials. The complex excitatory and inhibitory effects compose a closed loop, which responds to external stimuli by redistributing intrinsic and extrinsic connectivity.

However, this interpretation of interactions among neuronal modes within a cortical column and hierarchical information exchanges with external modes is a speculation that needs to be confirmed by more experimental data as well more reliable model estimates. Regardless of the role of external sources, the current results suggest that the modulation by external sources is necessary for describing the neural activities in the layer 2/3 of a barrel column during a localization task involving touches and whisking.

In summary, we (i) proposed a computational model for CaI signals using DCM, (ii) explored computational models to assess sensory perception through intrinsic and extrinsic connectivity, and (iii) examined the effective connectivity of the same neural circuit for different sensory perceptions (hit and error). We confirmed that a hierarchical architecture that has feed-forward and feed-backward connections is essential for formulating neural activity within a barrel cortical column for primary sensory perception. Both results of simulation and experimental analyses suggest the usefulness of DCM for utilizing CaI signals for the exploration of interactions among multitudes of neural activities observed in CaI or other imaging modalities.

Acknowledgement

This research was supported by Brain Research Program through the National Research Foundation of Korea funded by the Ministry of Science and ICT (NRF-2017M3C7A1049051). The authors thank the data distributor (https://crcns.org/data-sets/ssc/ssc-2) for sharing their experimental data. The authors thank the anonymous reviewers for their constructive comments. The authors also thank Karl Friston and Peter Zeidman for their informative guides.

Appendix A. Supplementary data

Supplementary data to this article can be found online at https://doi.org/10.1016/j.neuroimage.2019.116008.

References

Andermann, M.L., Moore, C.I., 2006. A somatotopic map of vibrissa motion direction within a barrel column. Nat. Neurosci. 9, 543–551.
Antic, S.D., Empson, R.M., Knopfel, T., 2016. Voltage imaging to understand connections and functions of neuronal circuits. J. Neurophysiol. 116, 135–152.
Aronoff, R., Matyas, F., Mateo, C., Ciron, C., Schneider, B., Petersen, C.C., 2010. Long-range connectivity of mouse primary somatosensory barrel cortex. Eur. J. Neurosci. 31, 2221–2233.
Bastos, A.M., Usrey, W.M., Adams, R.A., Mangun, G.R., Fries, P., Friston, K.J., 2012. Canonical microcircuits for predictive coding. Neuron 76, 695–711.
Berger, T., Borgdorff, A., Crochet, S., Neubauer, F.B., Lefort, S., Fauvet, B., Ferezou, I., Carleton, A., Luscher, H.R., Petersen, C.C.H., 2007. Combined voltage and calcium epifluorescence Imaging in vitro and in vivo reveals subthreshold and suprathreshold dynamics of mouse barrel cortex. J. Neurophysiol. 97, 3751–3762.
Chaudhuri, R., Knoblauch, K., Gariel, M.A., Kennedy, H., Wang, X.J., 2015. A large-scale circuit mechanism for hierarchical dynamical processing in the primate cortex. Neuron 88, 419–431.
Chen, T.-W., Wardill, T.J., Sun, Y., Pulver, S.R., Renninger, S.L., Baohan, A., Schreiter, E.R., Kerr, R.A., Orger, M.B., Jayaraman, V., et al., 2013. Ultrasensitive fluorescent proteins for imaging neuronal activity. Nature 499, 295–300.
Deco, G., Jirsa, V.K., Robinson, P.A., Breakspear, M., Friston, K., 2008. The dynamic brain: from spiking neurons to neural masses and cortical fields. PLoS Comput. Biol. 4, e1000092.
Douglas, R.J., Martin, K.A., 1991. A functional microcircuit for cat visual cortex. J. Physiol. 440, 735–769.
Douglas, R.J., Martin, K.A., 2004. Neuronal circuits of the neocortex. Annu. Rev. Neurosci. 27, 419–451.
Edelman, G.M., Gally, J.A., 2001. Degeneracy and complexity in biological systems. Proc. Natl. Acad. Sci. U. S. A. 98, 13763–13768.
Fischer, B.J., Anderson, C.H., Pena, J.L., 2009. Multiplicative auditory spatial receptive fields created by a hierarchy of population codes. PLoS One 4 e8015.
Freeman, W.J., 1975. Mass Action in the Nervous System: Examination of the Neurophysiological Basis of Adaptive Behavior through the EEG. Academic Press, New York.
Friston, K., 2018. Does predictive coding have a future? Nat. Neurosci. 21, 1019–1021. https://doi.org/10.1038/s41593-018-0200-7.
Friston, K., Mattout, J., Trujillo-Barreto, N., Ashburner, J., Penny, W., 2007. Variational free energy and the Laplace approximation. Neuroimage 34, 220–234.
Friston, K., Penny, W., 2011. Post hoc Bayesian model selection. Neuroimage 56, 2089–2099.
Friston, K., Zeidman, P., Litvak, V., 2015. Empirical bayes for dcm: a group inversion scheme. Front. Syst. Neurosci. 9.
Friston, K.J., 1994. Functional and effective connectivity in neuroimaging: a synthesis. Hum. Brain Mapp. 2, 56–78.

Friston, K.J., Harrison, L., Penny, W., 2003. Dynamic causal modelling. Neuroimage 19, 1273–1302.
Friston, K.J., Litvak, V., Oswal, A., Razi, A., Stephan, K.E., van Wijk, B.C.M., Ziegler, G., Zeidman, P., 2016. Bayesian model reduction and empirical Bayes for group (DCM) studies. Neuroimage 128, 413–431.
Gentet, L.J., Avermann, M., Matyas, F., Staiger, J.F., Petersen, C.C.H., 2010. Membrane potential dynamics of GABAergic neurons in the barrel cortex of behaving mice. Neuron 65, 422–435.
Gorski, J.A., Talley, T., Qiu, M., Puelles, L., Rubenstein, J.L.R., Jones, K.R., 2002. Cortical excitatory neurons and glia, but not GABAergic neurons, are produced in the emx1-expressing lineage. J. Neurosci. 22, 6309–6314.
Grewe, B.F., Langer, D., Kasper, H., Kampa, B.M., Helmchen, F., 2010. High-speed in vivo calcium imaging reveals neuronal network activity with near-millisecond precision. Nat. Methods 7, 399-U391.
Guo, Z.V., Li, N., Huber, D., Ophir, E., Gutnisky, D., Ting, J.T., Feng, G., Svoboda, K., 2014. Flow of cortical activity underlying a tactile decision in mice. Neuron 81, 179–194.
Haeusler, S., Maass, W., 2006. A statistical analysis of information-processing properties of lamina-specific cortical microcircuit models. Cerebr. Cortex 17, 149–162.
Helassa, N., Podor, B., Fine, A., Torok, K., 2016. Design and mechanistic insight into ultrafast calcium indicators for monitoring intracellular calcium dynamics. Sci. Rep. 6, 38276.
Hodgkin, A.L., Huxley, A.F., 1952. A quantitative description of membrane current and its application to conduction and excitation in nerve. J. Physiol. 117, 500–544.
House, D.R., Elstrott, J., Koh, E., Chung, J., Feldman, D.E., 2011. Parallel regulation of feedforward inhibition and excitation during whisker map plasticity. Neuron 72, 819–831.
Huber, D., Gutnisky, D.A., Peron, S., O'Connor, D.H., Wiegert, J.S., Tian, L., Oertner, T.G., Looger, L.L., Svoboda, K., 2012. Multiple dynamic representations in the motor cortex during sensorimotor learning. Nature 484, 473–478.
Jack, J.J.B., Noble, D., Tsien, R., 1975. Electric Current Flow in Excitable Cells. Clarendon Press, Oxford.
Jansen, B.H., Rit, V.G., 1995. Electroencephalogram and visual evoked potential generation in a mathematical model of coupled cortical columns. Biol. Cybern. 73, 357–366.
Kinnischtzke, A.K., Simons, D.J., Fanselow, E.E., 2014. Motor cortex broadly engages excitatory and inhibitory neurons in somatosensory barrel cortex. Cerebr. Cortex 24, 2237–2248.
Knight, B.W., 1972. Dynamics of encoding in a population of neurons. J. Gen. Physiol. 59, 734–766.
Lee, S., 2013. Pharmacological inhibition of voltage-gated Ca2+ channels for chronic pain relief. Curr. Neuropharmacol. 11, 606–620.
Liley, D.T.J., Cadusch, P.J., Dafilis, M.P., 2009. A spatially continuous mean field theory of electrocortical activity. Netw. Comput. Neural Syst. 13, 67–113.
Manita, S., Suzuki, T., Homma, C., Matsumoto, T., Odagawa, M., Yamada, K., Ota, K., Matsubara, C., Inutsuka, A., Sato, M., et al., 2015. A top-down cortical circuit for accurate sensory perception. Neuron 86, 1304–1316.
Markov, N.T., Vezoli, J., Chameau, P., Falchier, A., Quilodran, R., Huissoud, C., Lamy, C., Misery, P., Giroud, P., Ullman, S., et al., 2014. Anatomy of hierarchy: feedforward and feedback pathways in macaque visual cortex. J. Comp. Neurol. 522, 225–259.
Marreiros, A.C., Daunizeau, J., Kiebel, S.J., Friston, K.J., 2008. Population dynamics: variance and the sigmoid activation function. Neuroimage 42, 147–157.
Marreiros, A.C., Kiebel, S.J., Friston, K.J., 2010. A dynamic causal model study of neuronal population dynamics. Neuroimage 51, 91–101.
Mesulam, M.M., 1998. From sensation to cognition. Brain 121 (Pt 6), 1013–1052.
Meyer, H.S., Schwarz, D., Wimmer, V.C., Schmitt, A.C., Kerr, J.N., Sakmann, B., Helmstaedter, M., 2011. Inhibitory interneurons in a cortical column form hot zones of inhibition in layers 2 and 5A. Proc. Natl. Acad. Sci. U. S. A. 108, 16807–16812.
Mizrahi, A., Hirtzlin, T., Fukushima, A., Kubota, H., Yuasa, S., Grollier, J., Querlioz, D., 2018. Neural-like computing with populations of superparamagnetic basis functions. Nat. Commun. 9, 1533.
Moran, R., Pinotsis, D.A., Friston, K., 2013. Neural masses and fields in dynamic causal modeling. Front. Comput. Neurosci. 7, 57.
Newman, M.E.J., Girvan, M., 2004. Finding and evaluating community structure in networks. Phys. Rev. E 69.
Ohki, K., Chung, S., Ch'ng, Y.H., Kara, P., Reid, R.C., 2005. Functional imaging with cellular resolution reveals precise micro-architecture in visual cortex. Nature 433, 597–603.
Park, H.J., Friston, K., 2013. Structural and functional brain networks: from connections to cognition. Science 342, 1238411.
Pasupathy, A., Connor, C.E., 2002. Population coding of shape in area V4. Nat. Neurosci. 5, 1332–1338.
Penny, W.D., Stephan, K.E., Daunizeau, J., Rosa, M.J., Friston, K.J., Schofield, T.M., Leff, A.P., 2010. Comparing families of dynamic causal models. PLoS Comput. Biol. 6, e1000709.
Peron, S.P., Freeman, J., Iyer, V., Guo, C., Svoboda, K., 2015. A cellular resolution map of barrel cortex activity during tactile behavior. Neuron 86, 783–799.
Petersen, C.C.H., Sakmann, B., 2001. Functionally independent columns of rat somatosensory barrel cortex revealed with voltage-sensitive dye imaging. J. Neurosci. 21, 8435–8446.
Petreanu, L., Gutnisky, D.A., Huber, D., Xu, N.L., O'Connor, D.H., Tian, L., Looger, L., Svoboda, K., 2012. Activity in motor-sensory projections reveals distributed coding in somatosensation. Nature 489, 299–303.
Petreanu, L., Huber, D., Sobczyk, A., Svoboda, K., 2007. Channelrhodopsin-2-assisted circuit mapping of long-range callosal projections. Nat. Neurosci. 10, 663–668.
Pouget, A., Dayan, P., Zemel, R., 2000. Information processing with population codes. Nat. Rev. Neurosci. 1, 125–132.
Rahmati, V., Kirmse, K., Markovic, D., Holthoff, K., Kiebel, S.J., 2016. Inferring neuronal dynamics from calcium imaging data using biophysical models and bayesian inference. PLoS Comput. Biol. 12, e1004736.
Rosch, R.E., Hunter, P.R., Baldeweg, T., Friston, K.J., Meyer, M.P., 2018. Calcium imaging and dynamic causal modelling reveal brain-wide changes in effective connectivity and synaptic dynamics during epileptic seizures. PLoS Comput. Biol. 14, e1006375.
Rubinov, M., Sporns, O., 2010. Complex network measures of brain connectivity: uses and interpretations. Neuroimage 52, 1059–1069.
Shahriari, B., Swersky, K., Wang, Z., Adams, R.P., Freitas, N.d., 2016. Taking the human out of the loop: a review of bayesian optimization. Proc. IEEE 104, 148–175.
Sober, E., 1990. Explanation in Biology: Let's Razor Ockham's Razor, vol. 27. Royal Institute of Philosophy Supplements, pp. 73–93.
Spiegler, A., Kiebel, S.J., Atay, F.M., Knosche, T.R., 2010. Bifurcation analysis of neural mass models: impact of extrinsic inputs and dendritic time constants. Neuroimage 52, 1041–1058.
Tamamaki, N., Tomioka, R., 2010. Long-range GABAergic connections distributed throughout the neocortex and their possible function. Front. Neurosci. 4, 202.
Van Geit, W., Gevaert, M., Chindemi, G., Rossert, C., Courcol, J.D., Muller, E.B., Schurmann, F., Segev, I., Markram, H., 2016. BluePyOpt: leveraging open source software and cloud infrastructure to optimise model parameters in neuroscience. Front. Neuroinf. 10, 17.
Wang, C.T., Lee, C.T., Wang, X.J., Lo, C.C., 2013. Top-down modulation on perceptual decision with balanced inhibition through feedforward and feedback inhibitory neurons. PLoS One 8, e62379.
Wang, X.J., 2002. Probabilistic decision making by slow reverberation in cortical circuits. Neuron 36, 955–968.
Wilson, H.R., Cowan, J.D., 1972. Excitatory and inhibitory interactions in localized populations of model neurons. Biophys. J. 12, 1–24.
Yaksi, E., Friedrich, R.W., 2006. Reconstruction of firing rate changes across neuronal populations by temporally deconvolved Ca2+ imaging. Nat. Methods 3, 377–383.
Zagha, E., Casale, A.E., Sachdev, R.N., McGinley, M.J., McCormick, D.A., 2013. Motor cortex feedback influences sensory processing by modulating network state. Neuron 79, 567–578.
Zagha, E., Murray, J.D., McCormick, D.A., 2016. Simulating cortical feedback modulation as changes in excitation and inhibition in a cortical circuit model. eNeuro 3.